HAL
open science

Study of the effect of growth kinetic and nucleation law on grain structure simulation during gas tungsten arc welding of Cu-Ni plate

Alexis Chiocca, Fabien Soulié, Frédéric Deschaux-Beaume, Cyril Bordreuil

To cite this version:

Alexis Chiocca, Fabien Soulié, Frédéric Deschaux-Beaume, Cyril Bordreuil. Study of the effect of growth kinetic and nucleation law on grain structure simulation during gas tungsten arc welding of Cu-Ni plate. Welding in the World, 2019, 10.1007/s40194-019-00717-0 . hal-02064887

HAL Id: hal-02064887

https://hal.science/hal-02064887v1

Submitted on 12 Mar 2019

HAL is a multi-disciplinary open access archive for the deposit and dissemination of scientific research documents, whether they are published or not. The documents may come from teaching and research institutions in France or abroad, or from public or private research centers.

L'archive ouverte pluridisciplinaire **HAL**, est destinée au dépôt et à la diffusion de documents scientifiques de niveau recherche, publiés ou non, émanant des établissements d'enseignement et de recherche français ou étrangers, des laboratoires publics ou privés.

Study of the effect of growth kinetic and nucleation law on grain structure simulation during gas tungsten arc welding of Cu-Ni plate

A. Chiocca[1] · F. Soulié[1] · F. Deschaux-Beaume[1] · C. Bordreuil[1]

Abstract

The purpose of this article is to investigate the influence of growth kinetic models and nucleation models on the grain structure predicted by cellular automata (CA) during bead on Cu30Ni thin plate. Temperature field is obtained with the computation of two-dimensional finite element model (FE). Based on these temperatures, a CA model simulates the evolution of the envelope of grains along the solidification front. It is shown that for the same temperature field, the grains structure is modified if the growth model changes. The influence of the nucleation law parameters is also discussed from a modelling point of view. Experimental size of the weld pool are compared with thermal results and EBSD maps are compared with grain structure prediction obtained with the CA algorithm.

Keywords Grain structure · GTA welding · Binary alloy · Modelling · EBSD

1 Introduction: microstructure prediction in welding process

Arc welding is a common method to join one or two metallic materials by melting them with the help of the energy of an electric arc. The mechanical properties and the structural integrity of the assembly depend on the microstructure obtained after the solidification of the fusion zone. The size and shape of the grains as well as the microstructural factors such as dendrite spacing depend on thermal and solutal fields at the microscopic scale. Grain and dendrite morphologies in the mushy zone play also an important role in the material behaviour during the last stage of solidification specially concerning the hot cracking susceptibility [1].

Solidification mechanism of weld pool is complex and varies along the solid/liquid interface between the fusion line border and the centreline of the weld pool. Numerous parameters such as growth rate R, temperature gradient G, total undercooling ΔT and solutal gradient G_c can influence microstructure generation. All these variables are controlled by heat and mass transfers occurring during the process that can change with process parameters.

Grain structure formed in the fusion zone is driven by different mechanisms. Weld pool solidification begins by epitaxial growth from partially melt grains along the fusion zone boundary. These grains grow with the advancing weld pool from the fusion line boundary to the centre. Depending on thermal and solutal conditions, the dendrites grow more or less rapidly.

Thermal conditions in the centre of the weld pool can also promote nucleation of new grains. These new grains will grow and could outgrow other grains. This leads to a columnar to equiaxed transition (CET) in the grain structure morphology.

To predict grain structure with these complex solidification scenarios, advanced simulation techniques must be developed. Most popular methods used a welding process simulation to estimate thermal fields evolution in and near the weld pool combined with microstructural simulation. Pavlyk et al. [2] combined finite difference modelling with phase field model at the microstructural scale. Farzadi et al. [3] carried out the same kind of simulation and compared the obtained data with experimental results on a binary alloy. These methods are very powerful but cannot predict a transition between equiaxed and columnar grains morphology that plays an important role in hot cracking.

✉ C. Bordreuil
cyril.bordreuil@umontpellier.fr

[1] LMGC, Université de Montpellier, CNRS, Montpellier, France

A series of papers detailed the grain structure prediction based on Monte Carlo simulation [4] at the meso-scale. The results are interesting but this kind of evolution cannot integrate grain orientations accurately. Recently, Chen et al. [5] adapted a three-dimensional cellular automata-finite element (CAFE) method for welding simulations and used it to predict grain structure. Based on a dendritic growth law derived from a Kurz Giovanola Trivedi (KGT) model [6], Chen et al. [5] were able to predict epitaxial growth and grain growth selection even for multiple solidification/fusion cycles. In this important work, the nucleation phenomenon was not integrated despite its importance in CET prediction.

In order to investigate the relationship between process parameters and grain structure after solidification, Chiocca et al. [7] developed bead on plate experiments on a Cu-Ni binary alloy. In situ observations at the process scale and around the solid/liquid interface were carried out. Some EBSD measurements in the weld pool region demonstrated a strong influence of process parameters on the microstructure in the weld pool. The purpose of this paper is to simulate these experiments and to investigate the influence of the parameters entering in the growth kinetic and nucleation model that drive grain structure predictions in the CA model.

2 Modelling of grain structure formation during welding

Grain structure is generated during the solidification of the weld pool. Different phenomena are involved in weld solidification. Microscopic observations indicate that the microstructure is mainly columnar dendritic. Primary arms called also as dendrite trunks are solidifying along the heat flow direction. The solidified grain envelope depends then on the evolution of dendrite trunks under solutal and thermal flows. The modelling of the evolution of grain envelope can be based on growth kinetic laws that are generally driven by the total undercooling $\Delta T = T_{liq} - T(x, y)$ where T_{liq} is the liquidus temperature and $T(x, y)$ is the temperature at the dendrite tip. The total undercooling is due to different mechanisms near the dendrite tip (solid-liquid interface curvature, solutal gradient, latent heat of fusion,..) and is expressed as the sum of these different undercoolings. The temperature field induced by the welding process is heterogeneous, and a thermal simulation must be carried out to know the solidification thermal conditions.

2.1 Solidification mechanisms

Two different mechanisms occur during the bead solidification and affect the weld bead grain structure: the epitaxial grain growth and the nucleation of new grains. Grains grow under constrained solidification conditions that are driven by the temperature field induced by the process. During cooling under a constant temperature gradient, the grains grow by the displacement of primary dendrite arm tips following preferential crystallographic orientation, inside the undercooled liquid. Depending on the crystallographic orientations of dendrite trunk relative to the heat flow direction, some grains grow faster. This difference of growth velocity causes some grains to be overtaken by their neighbours and their growth is stopped, following a selective growth mechanism. In pure conduction mode and constant thermal gradient, the temperature of the dendrite tip is below the liquidus temperature due to the undercooling phenomena [8]. In this region, it is possible for different sites (inoculants or detached dendrite arms) to form a nuclei for a new grain.

In the case of varying thermal conditions such as in welding, selective grain growth is more complex. In the border of the weld pool, the growth occurs spontaneously by epitaxy from unmelted grains of the base material. Selection mechanism occurs at these times. Once selection has occurred, a new microstructure is obtained. Evolution of this new structure is driven by temperature field evolutions. Based on thermal conditions, equiaxed grains can nucleate in the undercooled liquid ahead of columnar grains leading to CET. Some models [9] relate the evolution of the solidification rate R and the thermal gradient G along the liquidus isotherm, in order to predict the nucleation ahead of columnar grains. These models give rapid insight of the presence of CET but are unable to predict grain size and grain selection.

In the next paragraph, some mesoscopic modelling for dendrite growth and nucleation are reviewed. These models are implemented in the cellular automaton algorithm to investigate grain selection based on parameters of grain growth and nucleation laws.

2.1.1 Grain growth

To model dendritic grain envelope, dendrite trunk growth must be modelled. During solidification process, the dendrite tip growth is generally modelled by a Kurz Giovanola Trivedi (KGT) model [6] based on the following equations:

$$\Omega = \frac{C_l - C_0}{C_l(1-k)} = Iv(Pe) \tag{1}$$

$$R = 2\pi\sqrt{\frac{\Gamma}{mG_c\zeta_c - G}} \tag{2}$$

$$\Delta T = mC_0\left[1 - \frac{1}{1-\Omega(1-k)}\right] \tag{3}$$

where $Pe = \frac{Rv_g}{2D_c}$ is the solutal Peclet number, Ω is the supersaturation, C_0 is the initial solute concentration of the alloy, C_l is the concentration in the liquid, k is the partition coefficient in the phase diagram, m is the slope of the liquidus line, D (D_c) is the thermal (solutal) diffusion coefficient, Γ is the Gibbs Thomson Energy, G is the thermal gradient imposed by the process, G_c is the solutal gradient in the liquid at the solid-liquid interface, ΔT is the total undercooling, R is the dendrite tip radius and v_g is the growth rate of the dendrite tip. ζ_c is a correcting factor introduced in rapid solidification [10].

The numerical resolution of the previous equations allows to obtain values of v_g for various ΔT that can be fitted by a polynomial expression:

$$v_g(\Delta T) = A\Delta T^n \tag{4}$$

where A and n are the fitting parameters.

Note that this model only takes into account the thermal and solutal diffusion effects. During welding, the liquid flow in the weld pool can modify the solutal and thermal gradients at the dendrite tip, and then modify the relation between the growth rate v_g and the total undercooling ΔT [10]. To take into account this phenomenon, the parameters (A and n) of the KGT model will be modified in the simulation section.

From a macroscopic point of view, the growth velocity v_g is related to the welding speed v_w all along the solidification front at the rear part of a quasi-stationary weld. If θ is the angle of the front normal relative to the welding direction and ψ is the angle of preferential crystallographic growth orientation relative to the normal of the front [11], the velocities are related by:

$$v_g = v_w \frac{cos\theta}{cos\psi} \tag{5}$$

This equation traduces that the growth is faster in the centreline of the weld pool ($\theta = 0$).

A welding speed of 4mm/s gives a growth rate of the same value at the centreline of the weld pool for crystallographic direction aligned with the centreline.

2.1.2 Nucleation law

Equiaxed grain nucleation is due to the activation of different sites inside the undercooled liquid. This physical phenomenon can be enhanced by the addition of inoculant or due to the detachment of dendrite tips due to the stirring in the liquid. These two phenomena can be modelled by a similar law of heterogeneous nucleation but the parameters would be quite different. For the case of inoculant, the parameters will depend on the chosen material, whereas in the case of dendrite tip detachment, it will depend on temperature and fluid flow. More the fluid flow is important more it can break dendrite tips and then increase the nucleation sites density.

For a given volume of liquid, a given number of sites can be activated depending on thermal conditions [12]. Heterogeneous nucleation in the bulk liquid is modelled using the approach proposed by Gandin et al. [8]. According to this model, sites are activated at a critical undercooling ΔT_0. Different sites of different sizes (either inoculant particles or dendrite tips) can be activated and the critical undercooling is different for each inoculant size. Nucleation model is based on nuclei density increase dn that is induced by an increase in the undercooling $d\Delta T$. The total density of grain can be approximated by a log-normal distribution [13]:

$$\frac{dn}{d\Delta T} = \frac{n_{max}}{\Delta T_\sigma \sqrt{2\pi}} \frac{1}{\Delta T} exp\left[-\frac{1}{2}(\frac{ln\Delta T - ln\Delta T_0}{\Delta T_\sigma})^2\right] \tag{6}$$

where n_{max} is the maximum grain density, ΔT_σ is the standard deviation and ΔT_0 is the total critical undercooling. By integrating (6), the total number of grains by volume unit is obtained. All these parameters can be determined with the help of macrography [12]. The most important parameter is the critical undercooling ΔT_0.

2.2 Thermal model

To estimate temperature field during the process, a heat transfer model based on energy conservation is developed:

$$\frac{\partial < \rho h >}{\partial t} - \nabla k \nabla T = \dot{Q} \tag{7}$$

where $< \rho h >$ is the average enthalpy, T is the temperature, k the thermal conductivity and $\dot{Q}$ is a volumic heat source. The average enthalpy depends on temperature, liquid and solid phase and composition of various phases that are neglected in the present work. The average enthalpy at a temperature higher than the liquidus is computed as a sum of sensible heat and latent heat:

$$if \quad T < T_S \quad < \rho h > = \rho_0 h_0 + \int_{T_0}^{T} \rho_s C_{ps} dT \tag{8}$$

$$if \quad T_S < T < T_l \quad < \rho h > = \rho_0 h_0 + \int_{T_0}^{T_s} \rho_s C_{ps} dT + f_l L \tag{9}$$

$$if \quad T > T_l \quad < \rho h > = \rho_0 h_0 + \int_{T_0}^{T_s} \rho_s C_{ps} dT + L + \int_{Tl}^{T} \rho_l C_{pl} dT \tag{10}$$

where C_{ps} is the solid specific heat, L the latent heat, C_{pl} the liquid specific heat, T_s the solidus temperature and T_l the liquidus temperature, $f_l = 1 - f_s$ is the liquid fraction,

Table 1 Parameters used in the thermal transient analysis

Liquid density (kg/m^3)	8110
Solid density (kg/m^3)	8940
Specific heat (solid state) $(J/kg/K)$	556
Specific heat (liquid state) $(J/kg/K)$	663
Thermal conductivity $(W/K/m)$	70
Volumetric latent heat J/m^3	$2.45.10^9$
Air exchange coefficient W/m^2K	10.
Clamping device exchange coefficient W/m^2K	10.e3
Liquidus temperature K (C)	1520 (1247)
Solidus temperature K (C)	1472 (1199)

Thermo-physical parameters are taken from [17]

ρ_s is the specific mass of the solid phase, ρ_l the specific mass of the liquid phase, ρ_0 and h_0 are respectively the specific mass and the enthalpy at ambient temperature (T_0). The solid fraction f_s of an alloy can depend on segregation during solidification. It was chosen to describe f_s by a Scheil-Gulliver law:

$$f_s = 1 - \left(\frac{T_s - T}{T_s - T_l}\right)^{\frac{1}{k-1}} \tag{11}$$

where k is the partition coefficient in the phase diagram at the liquidus temperature for the given solutal concentration and is assumed constant during the whole solidification [13].

Heat exchanges with the air and with the clamping device are modelled as boundary conditions using different exchange coefficients given in Table 1 and shown in Fig. 1. A thermal flux is imposed to model the heat input due to the arc (see section on simulation). With these boundary conditions, Eq. (7) is solved in the domain with finite element interpolation and a weak formulation for different time steps. The thermal field T_n is then known at time step t_n^{FE} at nodes of the mesh and can be used to simulate the grain structure in the cellular automaton. The temperature field is interpolated on cellular automaton following the natural neighbour interpolation method developed in [14].

2.3 Cellular automaton

In order to predict grain structure during welding process, a cellular automaton model is developed. The initial average grain diameter of the base material is around 100 μm and the initial grain structure is equiaxed in the whole specimen. It means that the CA grid should contain billions of cells per cm^3 that is cumbersome to manage [5] even with increasing high-performance computing. A two-dimensional model will be developed. It has the advantage to reduce the number of cells and let the analysis be manageable on a personal computer. To still reduce the computational time, the evolution of the grain structure is only investigated in a region of interest (Fig. 1).

To predict grain structure generation, the CA algorithm follows the development proposed by Gandin et al. [8]. First, fusion-solidification cycles have to be modelled ([14] and [5]). A state index is introduced to each cell in order to know the metal state. Different states indices are defined: Melt, Partially Melt and Solid. The Melt index indicates that the cell is inside the weld pool and the temperature is higher than the liquidus temperature. A Partially Melt cell is for cell on the edge of the weld pool or an equiaxed grain that has nucleated in the weld pool. Solid state cell indicates solidified cell or cell in the base material. During welding process, the sample is at low temperature before being melted by heat source. Cells in front of the weld pool are melted and cells at the rear of the weld pool are solidifying. Grain structure is generated in the rear and is driven by the undercooling. Grain growth begins on partially melted grains on the edges of the weld pool. State index can be changed from melt to partially melt and from partially melt to solid and from solid to melt when a cell becomes liquid.

2.3.1 Growth algorithm

As the grain microstructure is mainly columnar dendritic, the grain envelope can be delimited by the dendritic envelope that follows the dendrite tips growing on preferential crystallographic growth directions. As long as a two-dimensional model is chosen, only four directions are defined with the two Miller indices $< 10 >, < 01 >$ for

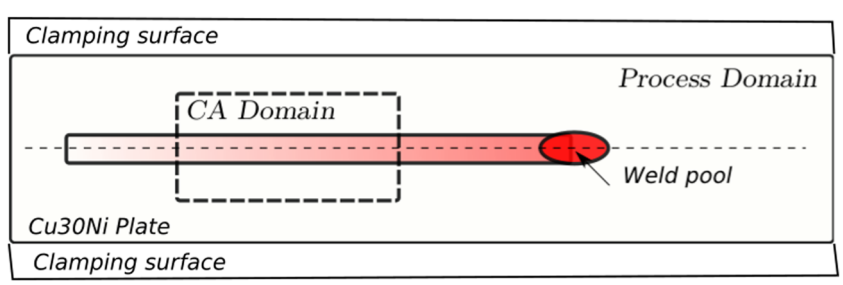

Fig. 1 Region of interest for the cellular automaton

growth directions. These directions are randomly tilted in the base material. The length of a dendrite is denoted as L_μ. One of those directions is related to the growth kinetic law of the dendrite tip by:

$$L_\mu(t) = \int_{t_0}^{t} v_g(\Delta T)dt \tag{12}$$

where t_0 is the time when growth starts. L_μ is also called extension. The algorithm to propagate the solid phase is based on dendritic extension L_μ in a cell. Based on the extension, the envelope is computed assuming a rectangle centred on the cell. A subscript i is added to identify one of the four directions. A superscript n is introduced to know the time step. The following explicit scheme is used to update extensions:

$$L_{\mu,i}^{n+1} = L_{\mu,i}^{n} + \frac{v_g(\Delta T)}{\sqrt{2}}\delta t \tag{13}$$

where δt is the time used for the evolution of the grain structure. In welding process conditions, the undercooling varies with time in a cell. The explicit approximation imposed to the time step must fulfill a condition to not overestimate extensions. It is common to use the following approximation [15]:

$$\delta t_{max} = \alpha min(l_{CA}/max(v_g(\Delta T)), \Delta t) \tag{14}$$

where δt is the CA time step, α is a factor between zero and one and l_{CA} is the size of a cell in the cellular automaton grid. This expression is chosen in order that the integral does not overpass l_{CA}.

The choice of δt_{max} is important because a difference in the integration approximation can lead to different extensions and then to different grain structures. δt is often one order of magnitude lower than the finite element thermal simulation. Time steps for the cellular automaton are denoted by t_k^{CA}.

The simple two-dimensional square algorithm to update extensions proposed by Gandin [8] is followed in order to prevent anisotropy problem due to cellular automaton geometrical grid on grain structure generation.

2.3.2 Nucleation algorithm

The management of nucleation can be cumbersome. Welding induces varying temperature field with cycles of melting-solidification. The distribution of sites in the bulk liquid based on nuclei density (6) cannot be used in the weld pool due to non-homogeneous thermal field. The best algorithm to treat nucleation is to work with a probability p_n of a cell to nucleate. This probability is derived from Eq. 6. To be independent of cell size, the probability to nucleate in a cell depend on $n(\Delta T)$ but also on the volume (surface) of a cell element (S_{cell}) [8]:

$$p_n = n(\Delta T)S_{cell} \tag{15}$$

in this case, $n(\Delta T)$ is the number of grains by surface unit. Its determination is based on experimental measurements.

The probability of a cell is computed for every cell with a melt state index and for cell not adjacent to a partially melt cell in order to not stop the growth. A random number r is computed for every cell lower than the liquidus temperature. This random number r is compared to the probability to have a nuclei in the cell. If $r < p_n$, then the cell is a site for nucleation. A cell that meets these requirements is considered to be nucleated if the cell is not captured by a growing cell. A nucleated cell changes its state index from Melted to Partially Melted and an arbitrary crystallographic orientation is assigned to the cell.

To couple nucleation and grain growth, the algorithm is developed as:

1. t_{begin} and t_{end} : time for the beginning and end of the thermal process simulation.
2. t_n^{FE} : finite element time steps.
3. T_n^{FE} : finite element temperature field at time steps t_n^{FE}.
4. For t_n^{FE} in range (t_{begin}, t_{end}):
   (a) Update temperature field T_n.
   (b) Interpolate fields T_n on cell at t_k^{CA}.
   (c) Compute undercooling for every cell in `Partially Melted` state.
   (d) Nucleate cells indicator at time t_k^{CA}.
   (e) t_k^{CA} : time for cellular automaton model.
   (f) For t_k^{CA} in range (t_n^{FE}, t_{n+1}^{FE}):
      (i) Find weld pool location.
      (ii) Find cells with temperature higher than T_l in weld pool.
      (iii) Compute elongations for cells.
      (iv) Compute grain growth and competition.
      (v) Change state for cells and nucleate cells.

To have low computational time, it was chosen to compute temperatures and undercooling in cells before entering in the growing algorithm. For similar considerations, the nucleation algorithm is done before evolving the grains. All the algorithms are then explicit and the time step condition is mandatory to have relevant CA results (14).

3 Material and process parameters

In this part, the main parameters and data used in simulations are explained.

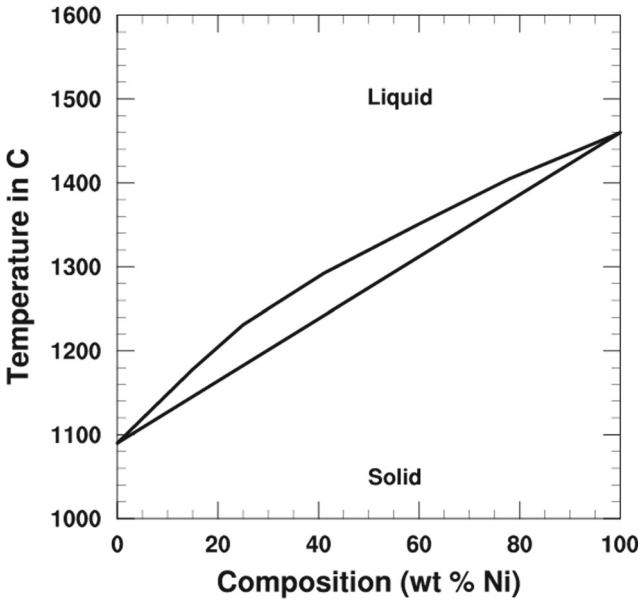

Fig. 2 Cu30Ni phase diagram [16]

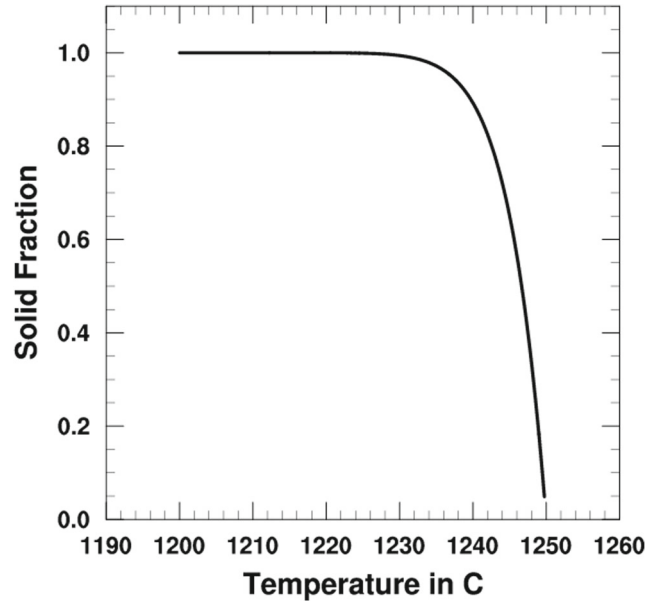

Fig. 4 Evolution of the enthalpy versus temperature

3.1 Material

The considered material is a Cu30Ni binary alloy. The Cu-Ni phase diagram is presented in Fig. 2.

For Cu30Ni, the solidus is around 1200 °C and the liquidus is around 1250 °C. Thermo-physical properties were found in [17]. It was assumed in the previous section that the material properties only depend on the solid fraction that depends on partition coefficient k (see Eq. 11). This coefficient can be estimated on equilibrium phase diagram (Fig. 2) around 1.4. Figure 3 presents the evolution of the solid fraction based on a Scheil-Guliver evolution and

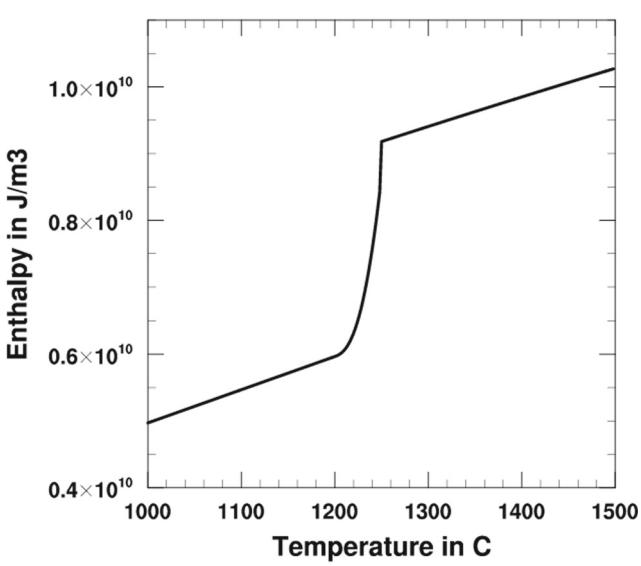

Fig. 3 Solid fraction versus temperature using the Scheil-Gulliver model

Fig. 4 presents the mass enthalpy computed from Eq. 8 for Cu30Ni. In Fig. 3, one can see that the solid fraction remains high above the solidus and decreases rapidly when approaching the liquidus. It means that according to the Scheil-Gulliver model, the latent heat is suddenly released around liquidus temperature.

The enthalpy is tabulated with respect to the temperature. All the parameters are summarised in Table 1.

The base material is modelled with an initial average grain diameter of about 100 μm. To generate the initial microstructure, a Delaunay mesh with the characteristic length around this value is created. Then, the Voronoï diagram is computed from the nodes of the mesh. A random crystallographic orientation is assigned to each Voronoï cell. This initial grain structure is used to assign the crystallographic orientation to the cells of a CA grid. The CA grid has a spacing (l_{CA}) of 25 μm. All computations conducted in the following are done on the same initial grain structure.

3.2 Growth modelling

Two different sets of parameters for Eq. 4 entering in Eq. 12 in the CA algorithm have been retained. The different sets are shown in Table 2.

Table 2 Parameters used for Kurz Giovanola Trivedi model in Eq. 4

	A	n
KGT1	2.55e-9	3.1
KGT2	5e-8	2

The first polynomial parameters (KGT1) are fitted from the resolution of Eqs. 1 and 2 and 3 using the equilibrium compositions of liquid and solid phases deduced from the phase diagram. With this growth model, a growth rate of 4mm/s, corresponding roughly to the growth rate in the centreline using process parameters J210, gives an undercooling of 90 °C. In welding, the fast solidification and the presence of fluid flow can decrease the growth rate, producing higher undercooling. So, the second law (KGT2) is chosen in order to get higher undercooling for the same growth rate. The parameters of KGT2 are chosen to give an undercooling around 300K for 4mm/s, as it can be encountered in fast solidification process (Fig. 5).

In the next, the two sets of parameters will be used in the cellular automaton to investigate the difference of grain structure prediction.

3.3 Nucleation

Two sets of parameters will be used for modelling heterogenous nucleation. These parameters are shown in Table 3. The first ΔT_0 parameter (NUCL1) is chosen in order to activate nucleation phenomena for a low undercooling (29K). The second value (NUCL2, 85K) is chosen in order to activate nucleation for undercooling just below the maximal undercooling obtained in the centreline when using a KGT1 growth model.

The evolutions of grain density in a cell given by the two laws are plotted in Fig. 6.

The n_{max} parameter is chosen to have around 16 grains by square millimetre. By multiplying this density by S_{cell} the surface of the cell, it gives the number of grains that can appear inside one cell for a given undercooling.

Table 3 Parameters used for heterogenous nucleation in Eq. 4

	$n_{max}\ grains/mm^2$	ΔT_0 (K)	ΔT_σ
NUCL 1	16	29	0.138
NUCL 2	16	85	0.138

3.4 Heat transfer modelling

A two-dimensional thermal finite element simulation is performed. The dimension of the plate is 250 x 100 x 1.6 mm. Only half of the plate is discretized due to the assumption of symmetry along the centreline.

The arc heat input to the workpiece is modelled as a flux with a Gaussian distribution:

$$q(r) = q_{max} exp\left(-3\left(\frac{\sqrt{(x-x_0)^2+(y-y_0-Vt)^2}}{r_0}\right)^2\right) \tag{16}$$

The parameter $q_{max} = \frac{\eta U I}{3\sqrt{\pi} r_0^2}$ is the maximum surface flux (W/m^2). It is related to process parameters arc voltage U, current I, the welding speed V, the process efficiency η and r_0 characterising the radius of the heat distribution. r_0 and η are identified from the width of the weld pool and from the thermal cycle recorded using a thermocouple positioned at 10mm from the centreline. Note that r_0 and η are constant for the two process parameters, so no adjustment was done between the two simulations.

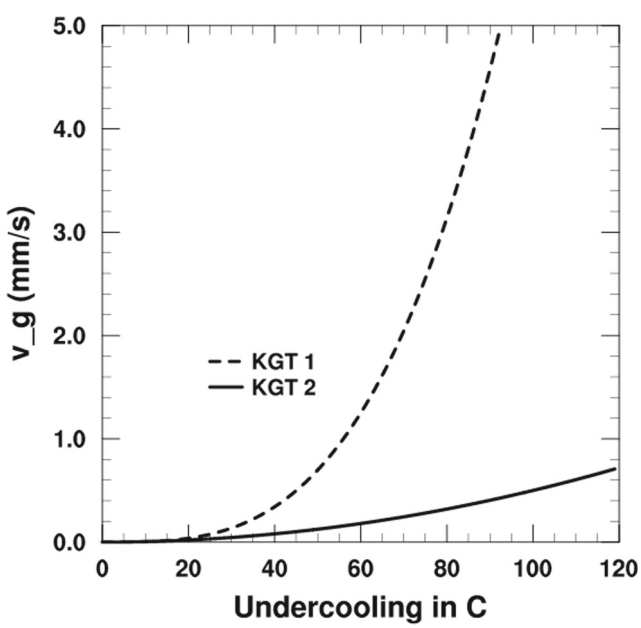

Fig. 5 Dendritic growth velocity in function of undercooling

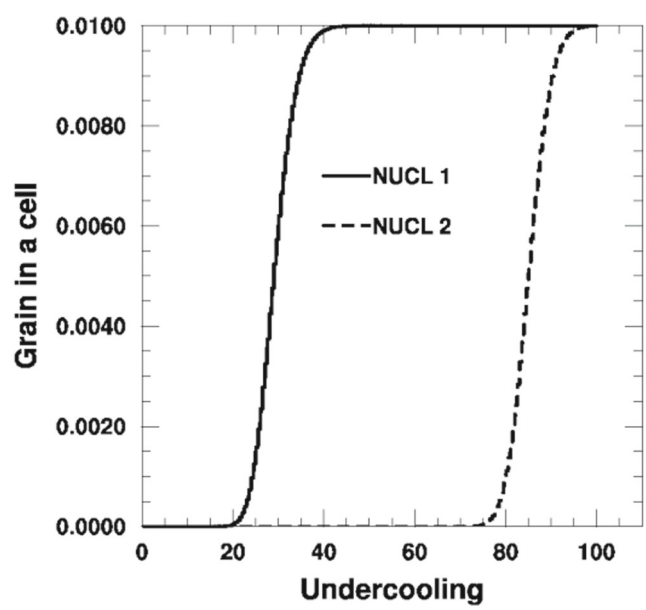

Fig. 6 Probability to have a grain in a cell in function of undercooling

Table 4 Process parameters used in the thermal transient analysis

	Current (A)	Arc voltage (V)	Welding speed (m/s)	Efficiency	r_0 (mm)
J210	90	10	0.0043	0.86	3
J300	90	10	0.003	0.86	3

Elements used for finite element simulation of the process are quadrangle quadratic isoparametric elements in the middle of the plate. An outer region is meshed with triangular quadratic elements. Boundary conditions are prescribed to simulate convection and radiation heat losses on all surfaces. Different groups are defined on the mesh to take into account exchange with the air or with the clamping device. The exchange coefficient is estimated with thermocouple measurements (see [18], in French). More details on the thermal transient analysis can also be found in [18].

Two parameter sets are retained named J210 and J300 with reference to the linear energy corresponding to each parameter set (Table 4). By increasing welding velocity, it is expected to change the shape and the size of weld pool, and to increase the cooling rate.

4 Results and discussions

In order to understand the coupling that can exist between the parameters of the kinetic law for dendritic growth, the nucleation activation and the grain structure prediction, simulations with different sets of parameters in the CA are used. To conclude this section, the grain structure predictions are compared with experimental results.

4.1 Temperatures and thermal gradients

The temperature field drives the evolution of the cellular automaton algorithm. Before investigating the effect of the modification of growth kinetic and nucleation models parameters (A, n, ΔT_0) on the grain structure, it is interesting to analyse thermal field and to study the solidification conditions along the solid-liquid interface. The purpose of this section is to analyse how the temperature field is modified with a change of 35% of the welding speed and discuss its possible influence on grain structure generation.

Thermal simulations can be divided in three parts: *(i)* the initiation phase for the three first seconds, *(ii)* the quasi-stationary phase and *(iii)* the ending phase (for the two last seconds). In phase *(ii)*, the shape of the weld pool does not have any evolution in a frame attached to the weld pool. Temperature results are extracted in this phase.

Based on the temperature field, the liquidus isotherm and the solidus isotherm can be positioned. It is assumed that at temperature higher than the liquidus isotherm, the material is fully liquid. For temperatures below the liquidus (1247 °C) for Cu30Ni, different states can be encountered. Below this temperature, the material remains liquid until the dendrite tip. The difference of temperature between the liquidus and the temperature at the tip of the dendrite corresponds to the total undercooling. Below the temperature at dendrite tips, the material is partially solidified, there is coexistence of liquid and solid phases. To simplify the weld pool boundary, it is supposed to correspond to the liquidus isotherm. To study the differences of temperatures and weld pool size, temperature profiles along two lines are extracted from simulations. The two lines start from the centre of the weld pool and goes to the edge for one line and to the rear of the weld pool following the centreline. The temperature profiles are plotted in Fig. 7 for the two sets of process parameters.

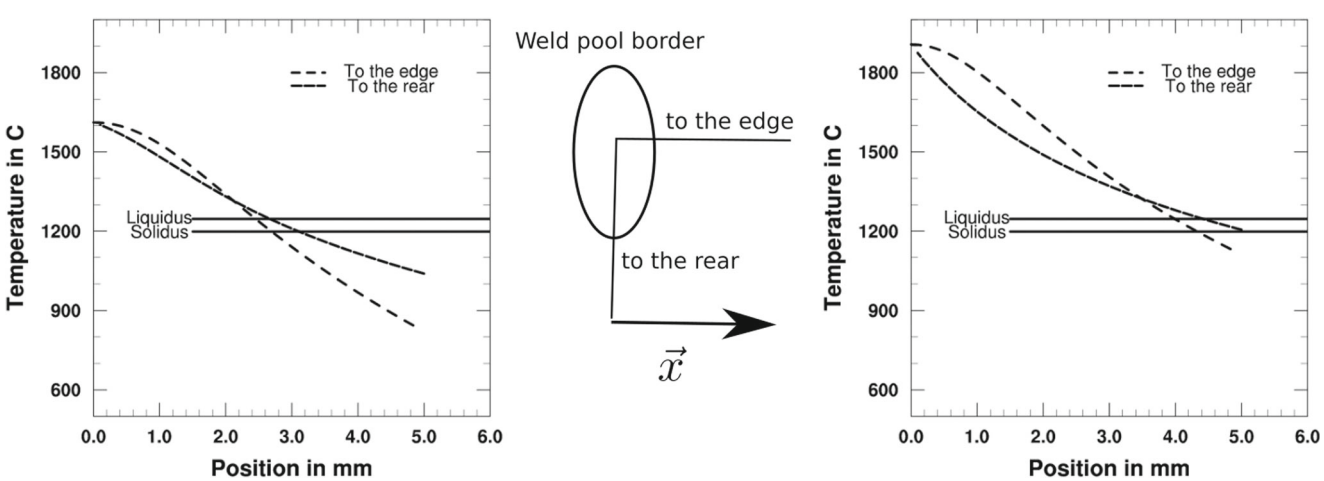

Fig. 7 J210 (left) and J300 (right) thermal results

The peak temperature in the centre of the weld pool exceeds 1800 °C for the J300 parameters and reaches 1600 °C for the j210 one. The temperature profile going to the rear crosses the liquidus temperature at a greater distance than the profile to the edge. It means that the weld pool is more elongated to the rear. The profiles give also an indication on the size of the solidification zone which is larger and longer for parameters J300. The temperature profile to the rear cuts the liquidus and solidus isotherms with a lower slope than to the edge. It means that the solidification zone will be larger at the rear of the weld pool. The slope between the liquidus and the solidus indicates that the gradient is higher at the edge than at the rear.

Another important quantity to investigate during solidification is the cooling rate (GR) to have information on the microstructural evolution. The cooling rate is extracted from the thermal simulations on points located on the liquidus contour from the edge to the rear of the weld pool. The cooling rates are compared for these two tests in Fig. 8.

The cooling rate reaches −200 °C/s for J300 and reaches −480 °C/s for J210 simulation at the rear of the weld pool at the centreline ($x = 0$). These results demonstrate the thermal modifications that occur when increasing the welding speed. It is interesting to remark that the relative increase of cooling rate is more important than the relative increase of welding speed because a contribution comes from the increase of the gradient near the liquidus. The location of the highest cooling rate is also the location of highest solidification rate due to the shape of the weld pool.

4.2 Influence of grain growth model

Before comparing the grain structures predicted for both retained process parameters, the influence of the growth kinetic model is discussed. Two different cellular automata simulations are computed using the growth model described in Section 2 and the thermal simulation results obtained with parameters set J210. Note that the nucleation modelling is not included in these simulations.

The grain structures at different time steps obtained using a KGT2 growth kinetic model are shown in Fig. 9. Because the model is two-dimensionnal, the crystallographic orientation is characterised by its angle composed to the normal to the welding direction. Each colour in Fig. 9 corresponds to an angle between $-\pi/4$ and $\pi/4$ to know the orientation of the crystallographic network. The blue (black) region in the centre corresponds to the weld pool. Cells in a melt state have no crystallographic orientation so an orientation of -1 is assigned. The weld pool shape tends to the tear drop shape encounters when the welding speed is high. This is due to the fact that a high undercooling is required with the KGT2 law to follow the isotherm displacement induced by the torch motion. It also indicates that the solidification front does not correspond to the liquidus isotherm. In Fig. 9, the colour of each cell corresponds to a crystallographic orientation θ of the $< 10 >$ direction. The grains are detected with cluster of cells with the same orientation. For this process parameter (J210), the shape of grains generated during welding is

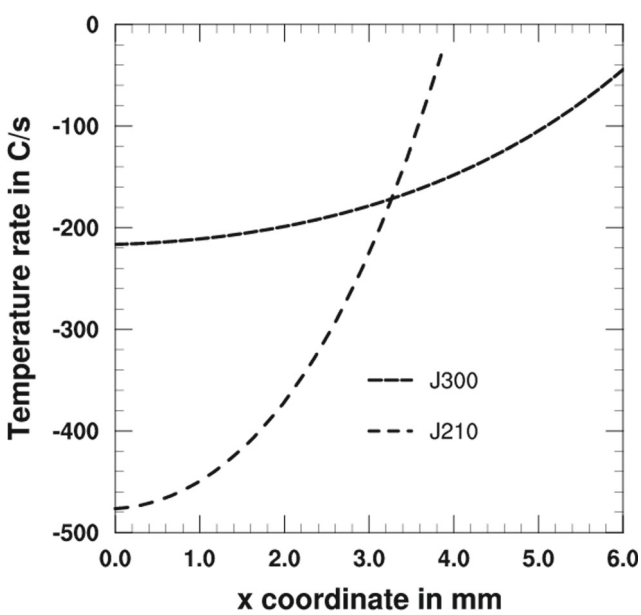

Fig. 8 Cooling rate along the liquidus isotherm for simulations J210 and J300. The coordinate $x = 0$ corresponds to the centre of the weld pool

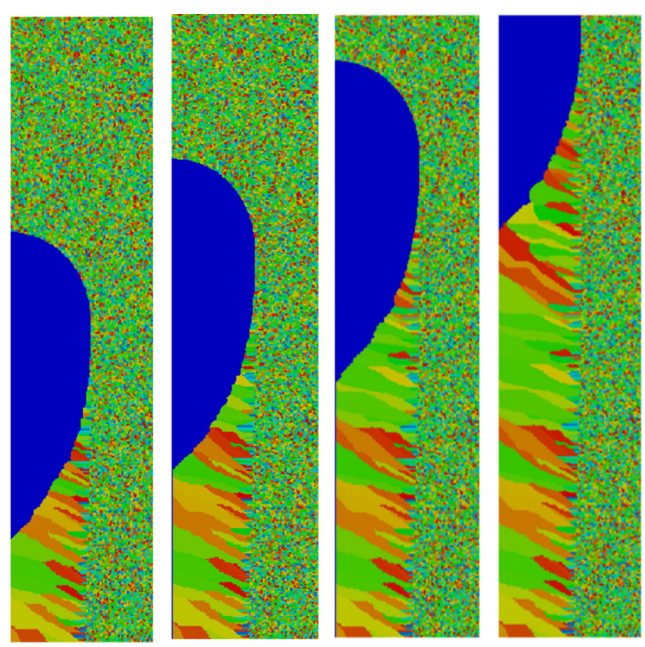

Fig. 9 Orientation of cells at different time steps for a cellular automaton simulation based on J210 thermal simulation and a KGT2 growth kinetic model

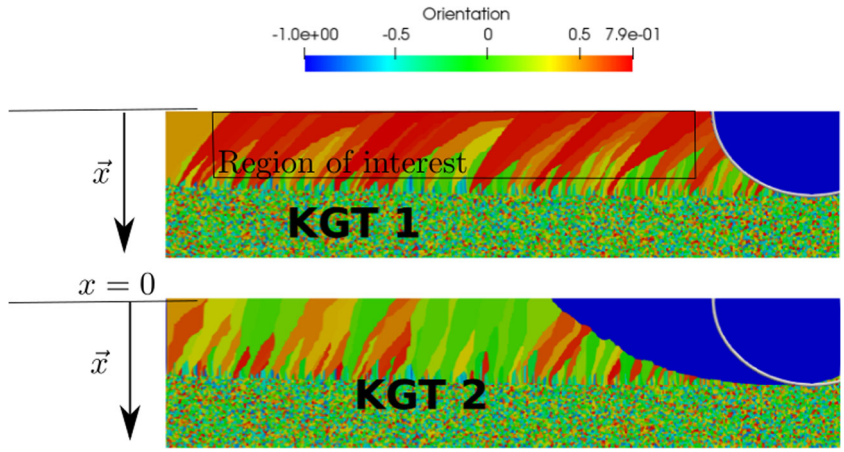

Fig. 10 Orientation of cells at the same time step for the different growth kinetic model (KGT1 and KGT2). The white line corresponds to the liquidus isotherm. The region were the grains are extracted is shown on the top images. Colour bar is valid for every simulation

elongated and tilted with respect to the welding direction. In Fig. 9, grain selection is very active at the edge of the weld pool. Once some grains are selected, they grow until they encounter grains coming from the other edge at the centreline of the weld pool.

Another simulation is carried out with a KGT1 grain growth model. The difference in grain structures can be seen in Fig. 10.

In Fig. 10, the weld pool obtained with the KGT1 model is less elongated than the one obtained with the KGT2 model. Due to the parameters of the KGT1 growth model, the dendrite tips grow for a lower undercooling, so dendrite tips are close to the liquidus isotherm. The weld pool shape for the KGT1 model looks more like an ellipse whereas the one with KGT2 looks like a tear drop geometry.

In Fig. 10, observations indicate that with the KGT1 model, crystallographic grain orientation are mainly defined with red colour. Red colour corresponds to a value of 45° between the $< 10 >$ crystallographic direction and the normal to the welding direction. For KGT2 parameters, green colour is more present and corresponds to an orientation of 25°. To compare more precisely the results in terms of grain structure, a region of interest is defined in the solidified area including for the two growth models, 25 grains. The grain size, the grain geometrical orientation, the crystallographic orientation and the misorientation along grain boundaries are extracted and compared for the two growth models. The grain size gives information on the selective grain growth. If the grains are large, it means that grains with a specific crystallographic orientation outgrow the others during solidification. Then, if they are small, it means that lots of grains can coexist. The geometrical orientation is computed from the angle of the principal axis of the grain relative to the normal of the welding direction. The geometrical orientation indicates the capacity of the grain to follow the heat flux.

Figure 11 shows that the KGT2 growth model gives a more homogeneous grain size distribution. It means that more grains are active and less grains with specific direction outgrow the others. In Fig. 12, one can see that the KGT

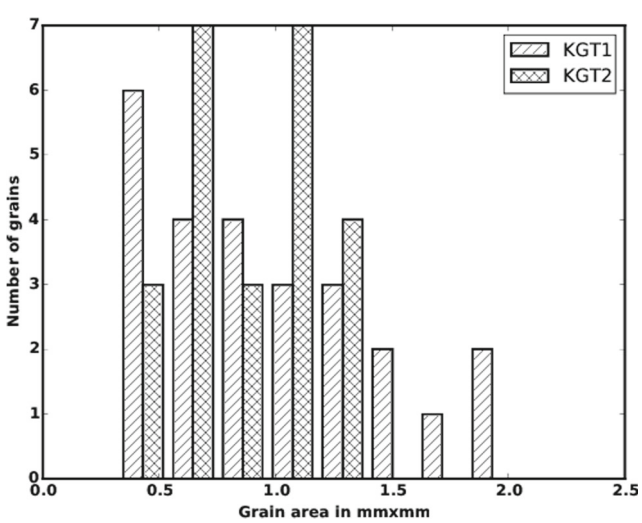

Fig. 11 Grain size for the two growth models

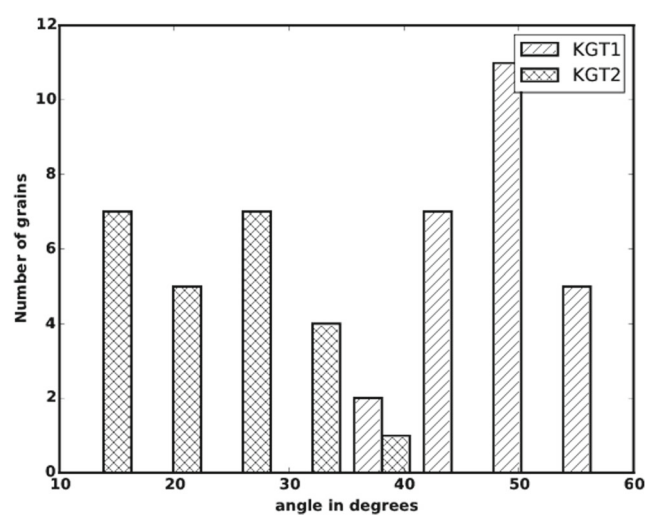

Fig. 12 Principal direction of grains for the two growth models

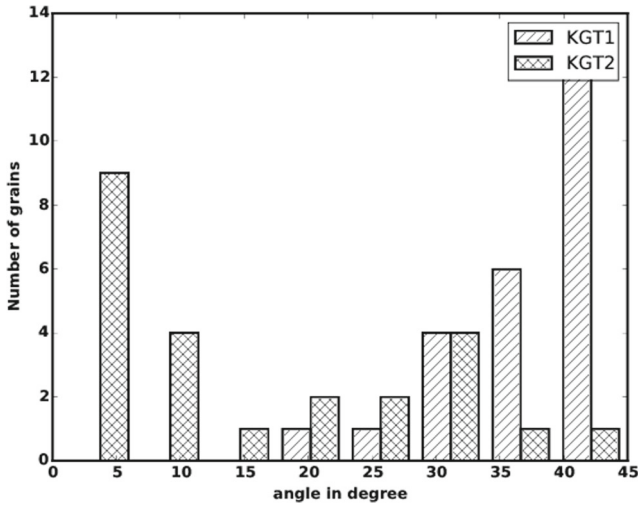

Fig. 13 Crystallographic orientations for the two growth models

1 model gives more grains whose principal axis is tilted to 45° relative to horizontal direction, that is correlated with the crystallographic direction given in Fig. 13. It means that grains with < 10 > tilted to 45° outgrow the others with this model. Once the grain competition is finished, it leads to large grain of 40° crystallographic direction that can follow the heat flow. For the KGT2 model, the distributions are more spread demonstrating less grain selection. All these remarks are confirmed qualitatively in Fig. 10. These results show the importance of the thermal conditions in the edge of the weld pool and its relation with the grain selection that occurs especially in the first stage of growth. With the KGT1 model, < 10 > grain directions aligned at 45° to the welding direction are boosted in the thermal fields and take the advantage over all the other orientations.

The last Fig. 14 shows misorientations. If lots of grains grow, there is more chance to have misorientation than

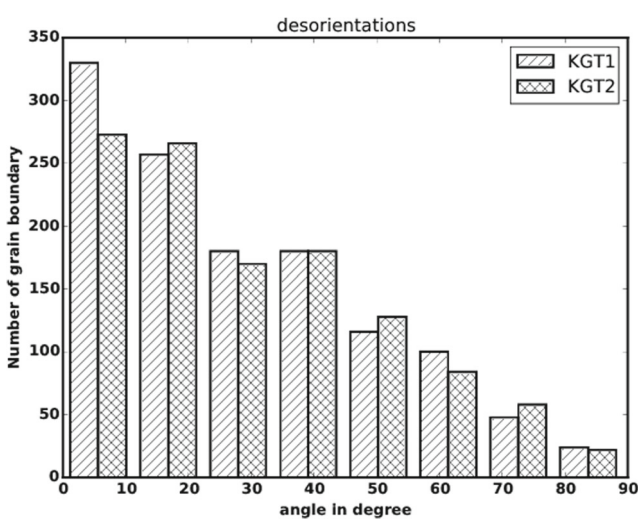

Fig. 14 Misorientation with the two growth models

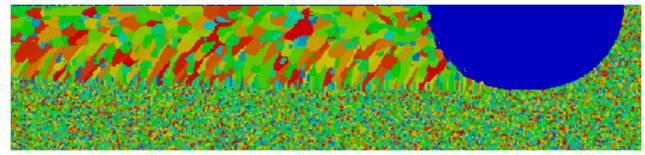

Fig. 15 Grain structure for KGT1 grain growth and Nucleation law Nucl1 ($\Delta T_0 = 29K$))

with few grains growing with the same crystalographic orientation.

To conclude, the results demonstrate that the grain growth model drives the grain selection for a given process parameter. The results show that higher is the growth velocity for a given undercooling, larger is the grain size distribution.

4.3 Influence of the nucleation model

To investigate the effect of the parameters of the nucleation model on the grain structure, two simulations are carried out using nucleation model parameters given in Table 3. The KGT1 growth kinetic model is selected both simulations. The nucleation and the grain growth are in competition in the generation of grain structures in the algorithm. The mechanisms are activated depending on the undercooling value.

Figures 15 and 16 present the results obtained with the two nucleation models.

The shape of the weld pool is the same for the two simulations because the same growth model was used. The grain structure obtained is equiaxed grains in the centre of the weld pool and columnar grains in the edge of the weld pool. The grain sizes in the centre are the same for both simulations. The grain sizes are directly linked to the parameter n_{max} that was kept identical for the two simulations. The results in Figs. 15 and 16 show a columnar to equiaxed transition (CET). The equiaxed zone has a half width of 1.8 mm for NUCL 1 model and 1.5 mm for NUCL2 model. The width of the equiaxed zone is linked to the "critical undercooling" parameter ΔT_0. More the critical undercooling is low, more the nucleation of new equiaxed grain can compete with the grain growth. The results shown in Figs. 15 and 16 indicate that the large difference of

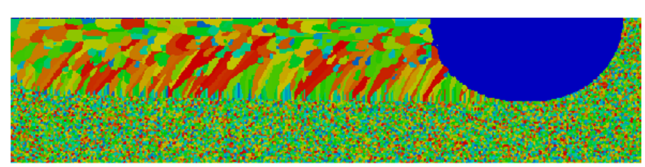

Fig. 16 Grain structure for KGT1 grain growth and nucleation law Nucl2 ($\Delta T_0 = 80K$)

undercooling leads to small change in the width of the equiaxed zone. It is interesting to remark the presence of equiaxed grains between neighbouring columnar grains in the two simulations. This is due to the random mechanism integrated in the nucleation algorithm.

4.4 Experimental results

Simulation results of grain structure predictions with the CA were compared with experimental results. Bead on plates using J210 and J300 welding parameters were carried out experimentally. After weld pool solidification, fusion zone were analysed using EBSD device (Jeol 5600). The results are shown in Figs. 17 and 18. Welding direction is from the bottom to the top. The colours represent crystallographic direction of one index relative to a fixed frame. The crystallographic grain orientation is three-dimensional but it can be used to determine grain size and geometric grain orientation.

In Figs. 17 and 18, the principal directions of grains are more tilted relative to the normal of the welding direction with the lower welding speed (J300). On both EBSD maps, the grain structure on the border of the weld pool reflects the epitaxy growth mechanism and the selective grain growth. The rapid solidification test J210 trapped more porosities (black disks) than the other test. The grain structure is mainly composed of columnar grains that

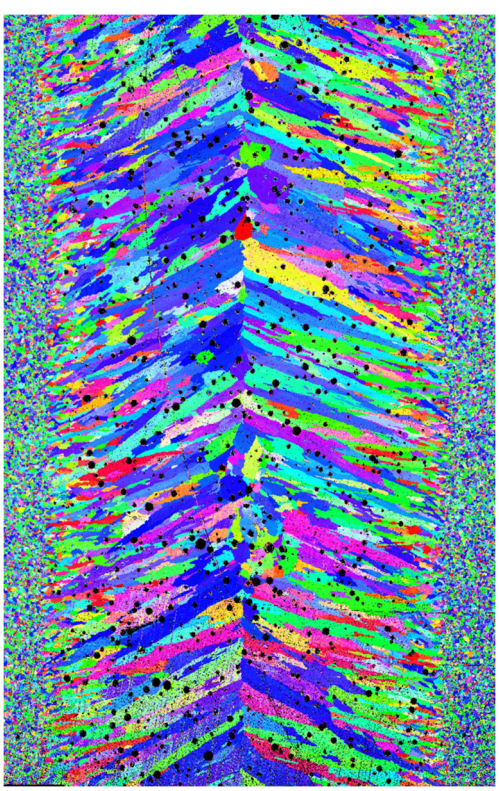

Fig. 17 EBSD grain structure for test J210

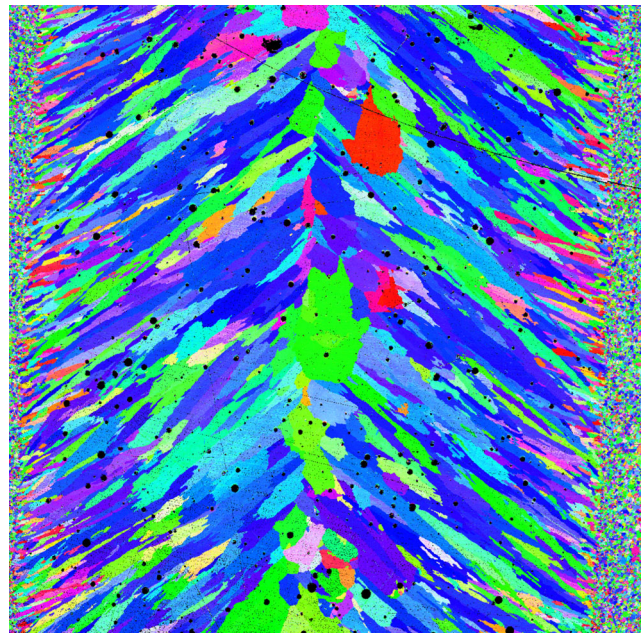

Fig. 18 EBSD grain structure for test J300. Black disks are porosities

encounter in the centre of the fusion zone. Columnar grains are relatively straight denoting the fact that grain envelope have difficulties to follow the isotherm under these process conditions. On these images (Fig. 18 in particular), some apparently equiaxed grains are observed in the middle of the fusion zone. For these grains, it is not straightforward to conclude if the grains were nucleated or if they are columnar coming from below the observing surface. The fact that Only few equiaxed grains are visible denotes that nucleation was not activated under these process conditions.

Figure 19 shows the orientation of the geometrical principal direction of the grains. The principal axis of the

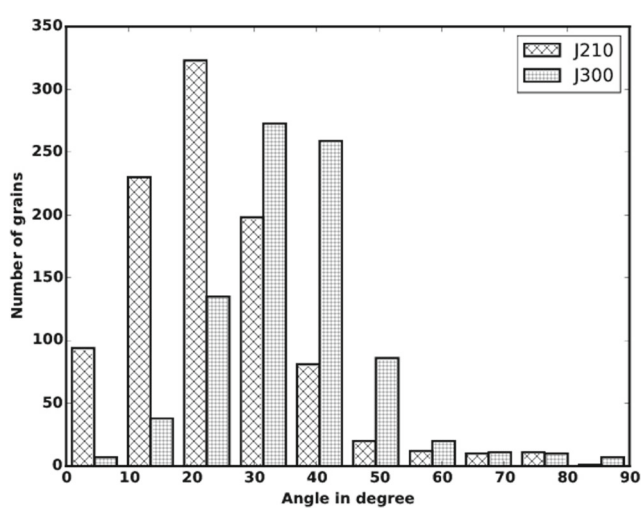

Fig. 19 Experimental grain principal geometrical direction relative to the normal of the welding direction

grains is less tilted for the test J210 than for the test j300. The angle between these directions and the normal to the welding direction is around 24° for J210 and around 35° for j300. This difference can be attributed to the capacity of the grain growth to follow the heat flow when the welding speed is lower. This capacity is driven by the growth kinetic model but also by the crystallographic orientation of the grains. This is the key point for grain selection. If grain selection occurs, some grains are trapped by other and cannot follow the isotherm. The remaining grains orientate easily in the direction of higher gradient because there is no other grains that outgrow their growing development.

The graph of Fig. 20 confirms the experimental observations on Figs. 17 and 18: grains are smaller for J210 tests. All these results confirm that grain selection is smaller for J210 test. A higher solidification rate leads to a higher number of grains that can grow. These grains are not necessarily the ones with the best orientation relatively to the heat flow.

4.5 Grain structure prediction

The comparison of the first simulation results with experimental results indicates that the KGT2 model seems to be more adapted for grain structure prediction for the two tests. Due to the almost absence of equiaxed grows experimentally observed, nucleation was not activated in the cellular automaton (CA) simulations. The results are shown in Figs. 21 and 22. The CA simulations are run for two different thermal simulations (J210 and J300). Experimental and simulated weld pool sizes are compared in Table 5. The experimental width and length are determined thanks to video recording [7]. The simulated width and length are determined thanks to the isocontour of the melt state index

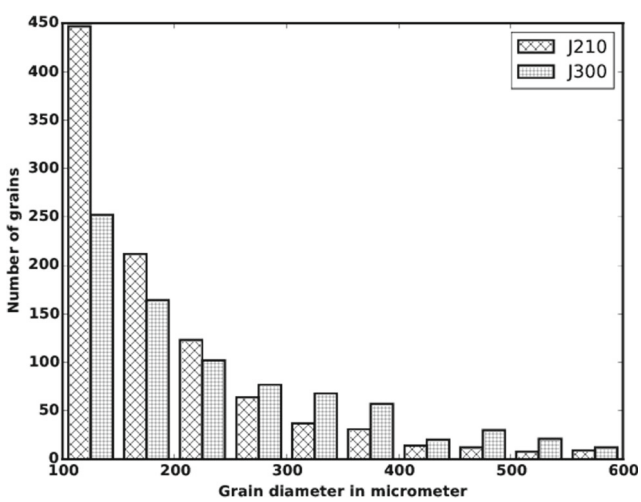

Fig. 20 Experimental grain mean diameter

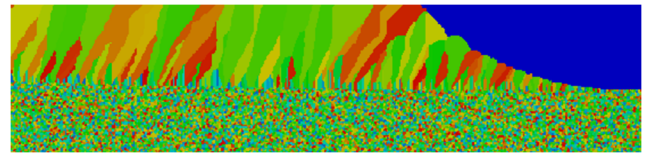

Fig. 21 Grain structure for the KGT2 grain growth model and j210 process parameters

and not from the liquidus isotherm as can be determined from thermal simulation.

The comparisons between the experimental and simulated widths are good. It is reminded that the process simulation parameters (efficiency η, r_0) are almost the same for J210 and J300. The difference between experimental and simulated results for the length can be attributed to the difficulty of measuring with accuracy the exact length on images in the rear of the weld pool but also to the difficulty for a thermal conductive model to take into account the effect of fluid flow in the weld pool on the other side. The difference of simulated and experimental length is larger for test J210. It comes probably from the fact that with increasing welding velocity, fluid motion becomes more important in the weld pool and can modify thermal transfer. These results indicate that the growth model driven by the temperature field obtained with the thermal simulation gives a good estimation to predict the solid-liquid boundary in the quasi-stationary zone.

The results in Figs. 21 and 22 present cell orientations relative to welding direction. As outlined earlier, cells with the same colour belong to the same grain. The CA domain is only a part of the process finite element simulation domain but side effects are not visible. Side effects can lead to unrealistic stray grain in the middle of the CA domain. With thermal conditions, this effect was not visible.

The CA simulation allows to investigate the grain distribution. For the two simulations, the morphology of the grain structure is composed of small grains at the edge of the bead. This is due to grain growth by epitaxy at the border. It is difficult to observe any grain size or grain orientation difference between the two simulations in these regions, then it is not possible to conclude on the influence of the grain growth law in this zone. In the rest of the bead, grains are larger for J300 simulation in particular when the

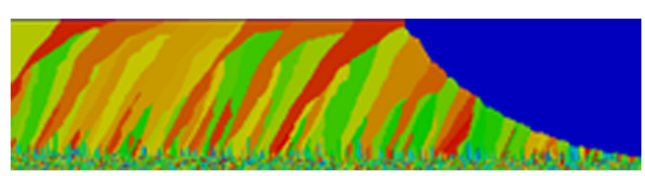

Fig. 22 Grain structure for the KGT2 grain growth model and j300 process parameters

Table 5 Comparison between simulated (Sim) and experimental (XP) weld pool shape with the KGT2 growth kinetic model

	Sim. width	Xp width	Sim. length	Xp length
J210	5.0	5.1	9.05	11.1
J300	8.04	8.0	14.05	15.2

columnar grains reach the centre of the weld. For J300 process parameters, the CA prediction gives principal axis of the shape of the grains more tilted than for J210. For this last one, geometry of the grains are less elongated and their main direction is orientated directly to the centre of the weld pool.

CA results give the same tendencies than the ones observed on EBSD maps. In order to confirm these observations, a region of interest is defined without the epitaxy zone on a CA grid in which grain size and grain direction are extracted. The results are shown in Figs. 23 and 24.

The grain size histograms are shown in Fig. 23. In the region of interest, respectively, 47 and 52 grains are analysed for J210 and J300 simulations. The mean value of grain geometrical orientation is 22° for J210 and 33° for J300. This is quite close to experimental results of Section 4.4. The results are more spread around the mean value for simulation results, it is probably due to the higher number of grains in the region of interest.

Concerning grain size, the highest bars are related to the same grain size (0.1 mm^2) for both process parameters but the distribution is not the same. The grain size distribution is more homogeneous for the J300 condition while most grains are small for the J210 condition. It is in agreement with experimental observations that showed the grains are smaller for J210 condition.

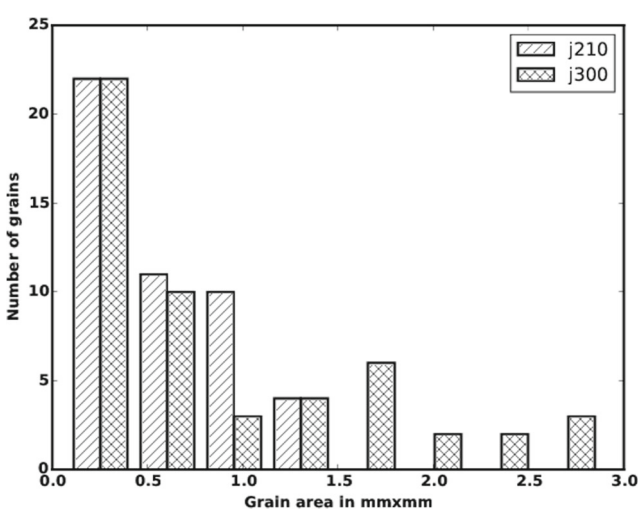

Fig. 23 Grain size for the different process parameters

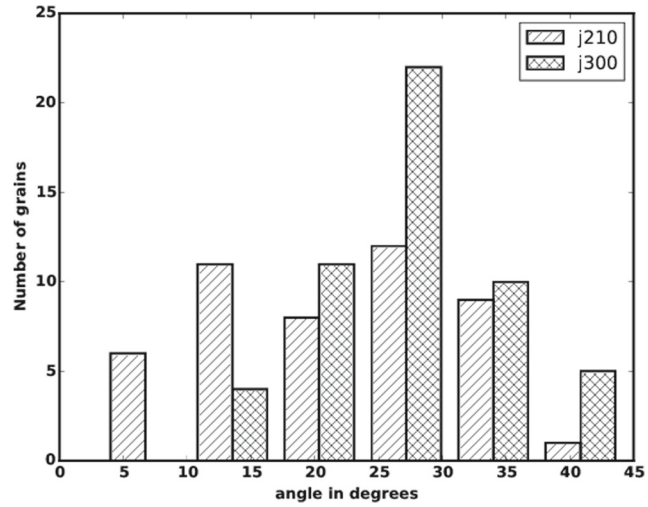

Fig. 24 Principal direction of grains for the different process parameters

5 Conclusion

The purpose of the paper was to investigate the influence of the models entering in the CA algorithm and thermal fields from the simulation of the process on the grain structure prediction. The thermal model is simple as it considers a plane thermal model and plane cellular automaton geometry. The current model allows to predict tear drop shape of the pool if growth kinetic model is well chosen. It approaches experimental results observed with EBSD measurements that give geometry of the grains. There is good agreement for the general shape, size and orientation of grains between experimental measurement and the model developed in the paper. The comparison of grain structures obtained with different grain growth model demonstrated the importance of grain selection mechanism. The paper investigates also the coupling between nucleation and grain growth. Nucleation models were tested and their capacity to predict columnar to equiaxed transition was demonstrated. Different results as well as temperature profiles ask the question of influence of fluid flow. To improve the prediction quality, the fluid flow has to be considered and in particular its influence in the energy equation. A strong coupling between mass and heat flow, and growth of grains will significantly make the modelling more complex.

Funding information All authors belong and were funded by the Université of Montpellier. Université de Montpellier is a university devoted to education and scientific research.

Compliance with ethical standards

Conflict of interest The authors declare that they have no conflict of interest.

References

1. Kou S (2003) Welding metallurgy. Wiley
2. Pavlyk V, Dilthey U (2004) Simulation of weld solidification microstructure and its coupling to the macroscopic heat and fluid flow. Model Simul Mater Sci Eng 12:33–35
3. Farzadi A, Do-Quang M, Serajzadeh S, Kokabi A, Amberg G (2008) Phase field simulation of weld solidification microstructure in an Al Cu alloy. Model Simul Mater Sci Eng, 16. https://doi.org/10.1088/0965-0393/16/6/065005
4. Rodgers TM, Mitchell JA, Tikare V (2017) A Monte Carlo model for 3D grain evolution during welding. Modell Simul Mater Sci Eng 25(6). https://doi.org/10.1088/1361-651X/aa7f20
5. Chen S, Guillemot G, Gandin Ch-A (2014) 3D coupled cellular automaton- finite element modeling for solidification grain structures in gas tungsten arc welding. ISIJ Int 54:401–407
6. Kurz W, Giovanola B, Trivedi (1986) Theory of microstructural development during rapid solidification. Acta Metallur 34:p823–830
7. Chiocca A, Soulié F, Bordreuil C, Deschaux-Beaume F (2016) In situ observations and measurements during solidification of CuNi weld pools. Sci Technol Weld Join 21(7):578–584
8. Gandin Ch-A, Rappaz M (1994) A coupled finite element-cellular automaton model for the prediction of dendritic grain structures in solidification process. Acta Metallur Materiala 42:2233–2246
9. Hunt JD (1948) Steady state columnar and equiaxed growth of dendrites and eutectic. Material Sci Eng 25:65–75
10. Takatani H, Gandin Ch-A, Rappaz M (2000) EBSD characterisation and modelling of columnar dendritic grains growing in the presence of fluid flow. Acta Materiala 48:675–688
11. Vitek JM (2005) The effect of welding conditions on stray grain formation in single crystal welds. Acta Materiala 53:53–67
12. Villaret V, Deschaux-Beaume F, Bordreuil C (2016) A solidification model for the columnar to equiaxed transition in welding of a Cr-Mo ferritic stainless steel with Ti as inoculant. J Mater Process Technol 233:115–124
13. Dantzig G, Rappaz M (2009) Soldification. CRC Press
14. Bordreuil C, Niel A (2014) Modelling of hot cracking in welding with a cellular automaton combined with an intergranular fluid flow model. Comput Mater Sci 82:442–450
15. Rappaz M, Gandin Ch-A, Desbiolles J-L, Thevoz P (1996) Prediction of grain structures in various solidification processes. Metallur Mater Trans A 27:695–705
16. Miettinen J (2003) Thermodynamic description of the Cu–Ni–Sn system at the Cu–Ni side. Comput Coupling Phase Diagrams Thermochem 27:309–318
17. Hupf T, Cagran C, Kaschnitz E, Pottlacher G (2010) Thermophysical properties of five binary copper-nickel alloys. Int J Thermophys 31:966–974
18. Chiocca A (2016) Phd Thesis. Univerisité de Montpellier